Mechanical forcing of convection by cold pools: collisions and energy scaling.

Bettina Meyer[1] and Jan Olaf Haerter[1]

[1]Niels Bohr Institute, University of Copenhagen

November 24, 2022

Abstract

Forced mechanical lifting through cold pool gust fronts can trigger new convection, and previous work highlights the role played by collisions between cold pools. However, as conceptual models show, the emergent organisation from two versus three colliding cold pools differs strongly. In idealised dry large-eddy simulations we therefore examine which of the two processes dominates. We simulate the spread of gravity currents and the collisions between two and three cold pools. The triggering likelihood is quantified in terms of the cumulative vertical mass flux of boundary layer air and the instantaneous updraft strength, generated at the cold pool gust fronts. We find that cold pool expansion can be well described by initial potential energy and time alone. Cold pool expansion monotonically slows but shows an abrupt transition between an axi-symmetric and a broken-symmetric state – mirrored by a sudden drop in expansion speed. We characterize these two dynamic regimes by two distinct power-law exponents and explain the transition by the onset of 'lobe-and-cleft' instabilities at the cold pool head. Two-cold pool collisions produce the strongest instantaneous updrafts in the lower boundary layer, which we expect to be important in environments with strong convective inhibition. Three-cold pool collisions generate weaker but deeper updrafts and the strongest cumulative mass flux and are thus predicted to induce the largest mid-level moistening, which has been identified as a precursor for the transition from shallow to deep convection. Combined, our findings may help decipher the role of cold pools in spatially organising convection and precipitation.

Mechanical forcing of convection by cold pools: collisions and energy scaling.

Bettina Meyer [1] and Jan O. Haerter [1,2,3]

[1] Niels Bohr Institute, University of Copenhagen, Blegdamsvej 17, 2100 Copenhagen, Denmark
[2] Complexity and Climate, Leibniz Center for Tropical Marine Research, Fahrenheitstrasse 6, 28359 Bremen, Germany
[3] Jacobs University Bremen, Campus Ring 1, 28759 Bremen, Germany

Key Points:

- A cold pool's initial potential energy is a good predictor of its spreading dynamics,
- Cold pool radii evolve as a combination of two power laws, highlighting a dynamic transition induced by 'lobe-and-cleft' instabilities,
- Updrafts and mass flux are strongly enhanced in multi-cold pool collisions compared to single cold pool gust fronts.

Corresponding author: Bettina Meyer, `bettina.meyer@nbi.ku.dk`

Abstract

Forced mechanical lifting through cold pool gust fronts can trigger new convection, and previous work highlights the role played by collisions between cold pools. However, as conceptual models show, the emergent organisation from two versus three colliding cold pools differs strongly. In idealised dry large-eddy simulations we therefore examine which of the two processes dominates. We simulate the spread of gravity currents and the collisions between two and three cold pools. The triggering likelihood is quantified in terms of the cumulative vertical mass flux of boundary layer air and the instantaneous updraft strength, generated at the cold pool gust fronts. We find that cold pool expansion can be well described by initial potential energy and time alone. Cold pool expansion monotonically slows but shows an abrupt transition between an axi-symmetric and a broken-symmetric state – mirrored by a sudden drop in expansion speed. We characterize these two dynamic regimes by two distinct power-law exponents and explain the transition by the onset of 'lobe-and-cleft' instabilities at the cold pool head. Two-cold pool collisions produce the strongest instantaneous updrafts in the lower boundary layer, which we expect to be important in environments with strong convective inhibition. Three-cold pool collisions generate weaker but deeper updrafts and the strongest cumulative mass flux and are thus predicted to induce the largest mid-level moistening, which has been identified as a precursor for the transition from shallow to deep convection. Combined, our findings may help decipher the role of cold pools in spatially organising convection and precipitation.

Plain Language Summary

The arrival of a convective thunderstorms is often announced by strong and cold wind gusts that can be felt by an observer at the surface. These gust fronts constitute the outer edge of convective cold pools, which are formed underneath clouds when part of the rain re-evaporates before reaching the surface, thereby cooling the sub-cloud air. In recent years, these cold pools have received increasing attention due to their role in triggering new convective rain events. Cold pools thereby affect the spatial location and timing of clouds and rain events. In this study we use a high-resolution numerical model to study the life cycle of single cold pools and their collision with other cold pools. We assume that the likelihood of triggering new convective events is proportional to (i) the strength of the vertical wind gusts that are produced at the cold pool gust front and where cold pools collide and (ii) how much moisture can be transported upwards above a height where the water condenses and forms clouds. We show that both these factors are strongly increased where two or more cold pools collide, highlighting the importance of the representation of cold pool collisions in climate models.

1 Introduction

Convective cold pools (CP) form when rain re-evaporates in the boundary layer below a (deep) convection cloud (J. Simpson, 1980; Droegemeier & Wilhelmson, 1985). The evaporation locally cools the air beneath the cloud, resulting in a density increase (Markowski & Richardson, 2010). Gravity accelerates the dense air towards the surface, where the cold air spreads horizontally as a gravity current, in this context referred to as CP. As laboratory and numerical investigations show, CPs can be seen as consisting of (i) a deeper head at the leading edge (approximately 500 m), separated by a turbulent wake from (ii) a thin cold air 'carpet' in the interior (Benjamin, 1968; Droegemeier & Wilhelmson, 1987; Kneller et al., 1999). The CP head characteristically is twice as deep as the interior (J. E. Simpson, 1972; J. Simpson, 1980; Markowski & Richardson, 2010), containing most of the cold air and moisture from rain re-evaporation. A CP can further be characterised by its volume, propagation speed of the head, lifetime, and density, where density derives from both temperature and moisture anomalies. The CP's circulation can be decomposed into a shallow flow, directed radially away from the CP center and causing the horizontal expansion of the CP, and a turbulent and rotational circulation within the CP head (Droegemeier & Wilhelmson, 1987; Rotunno et al., 1988; Cafaro & Rooney, 2018).

As a CP spreads along the surface, the radial density gradient and the radial motion create a narrow band of horizontal convergence of the near-surface wind field, which due to continuity requires pronounced updrafts in the atmospheric boundary layer aloft. These updrafts can lift the moist near-surface air to higher levels above the level of free convection (LFC) and moisten the upper boundary layer and lower troposphere, thereby triggering new convective events — an effect referred to as *mechanical* (or dynamical) forcing (Torri et al., 2015). In particular under suppressed conditions with pronounced convective inhibition (CIN), this mechanical forcing may represent a major contribution to convection triggering. Especially in CPs over the ocean, the likelihood of convective triggering is further enhanced by an incremented moisture concentration in the CP head, referred to as *thermodynamic* forcing (Addis et al., 1984; Tompkins, 2001b; Feng et al., 2015; Langhans & Romps, 2015). Both the thermodynamic and mechanical effect are enhanced when CPs collide (Droegemeier & Wilhelmson, 1985; Feng et al., 2015), where the latter is quantified in this study. Observational and numerical studies suggest, that the triggering of convection is enhanced when CPs collide (Feng et al., 2015; Kurowski et al., 2018; Torri & Kuang, 2019). Feng et al. (2015) found that the mean cloud fraction is increased by 70% along CP collision lines compared to single gust fronts.

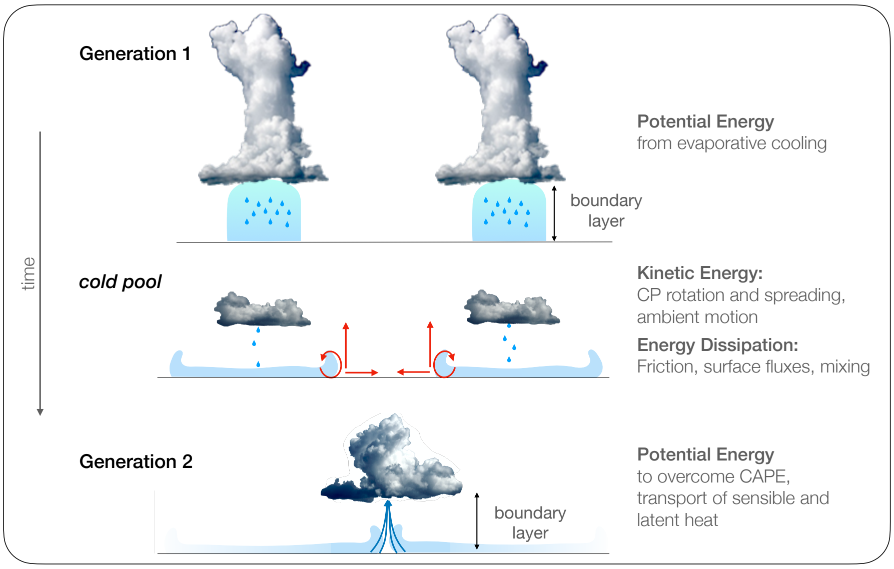

Figure 1. Simplified schematic of CPs linking convective events over space and time by converting the initial potential energy from evaporatively cooled air into kinetic energy of a CP, which by triggering convection transfers it back to potential energy of a second generation event.

Enhancing convective triggering by carrying energy and moisture, CPs can be understood as a link between clouds across time and space (Fig. 1): rain from a generation 1 convective cloud generates a CP, thereby moistening the air and transforming latent heat into potential and kinetic energy of the CP. Most of this energy and moisture (contributing to buoyancy) are contained in the CP head. As the CP spreads, energy and moisture are redistributed horizontally and vertically through lateral expansion and gust front dynamics. Thanks to this spatio-temporal link, CPs affect not only the cloud cover's local properties but also shape its meso-scale organisation. Given an ensemble of generation 1 convective cells and corresponding CPs, generation 2 convective cells appear to be non-randomly connected to the present ones, leading to the emergence of complex, non-random, organisational patterns (Purdom, 1976; Torri & Kuang, 2019; Haerter et al., 2019, 2020). Simple geometric models reveal that if the collision of any pair of two CPs yields a new convective cell, and thus a new CP, the number density of CPs inevitably increases and even diverges with time (Nissen & Haerter, 2020). Restricting such a model, conversely, to initiate new rain cells only where three distinct CP gust fronts collide, the population of CPs decreases over time — leading to a scale increase, when measuring typical distances between rain cells (Haerter et al., 2019). Hence, a better understanding of when and why two or three CPs are required for initiation of a new event is invaluable for properly capturing organisation effects in climate models.

In the atmospheric boundary layer the thermodynamic fields are vertically well mixed with small fluctuations, while the vertical velocity can show pronounced turbulent structure. This implies that thermodynamic perturbations show less sensitivity to model resolution than the dynamic ones (e.g., vertical velocity) (Hirt et al., 2020) and can be reasonably captured at the kilometer-scale of convection-resolving models (Leutwyler et al., 2016). Therefore, in this paper we focus on CP dynamics and the mechanical lifting. We do so by considering purely dry atmospheres, where CPs are characterised solely by a temperature anomaly, while moisture is neglected. We do this by running numerical high-resolution simulations.

In such a dry setting, a CP's effectiveness of triggering new convection is determined by the strength of the circulation – updrafts and connected overturning circulation – it induces in its environment. This circulation is proportional to the CP's height and propagation velocity, where, according to a long line of numerical and conceptual studies, the latter can be related to the temperature anomaly and height of the CP (Benjamin, 1968; Rooney, 2015, 2018; Grant & van den Heever, 2016). Thus, it is important to understand how the CP height and temperature anomaly scale with the size and strength of the initial rain event and evolve in time. In the simplest case a steady-state solution is assumed, allowing to relate the CP's propagation speed to the density and height of the CP head, as an estimate of the CP's potential energy (Benjamin, 1968). Such a situation can be generated by using a continuous forcing as in Droegemeier and Wilhelmson (1987), who studied the scaling in terms of the horizontal extent, height, and temperature of the initial cold air anomaly. However, in regards to modelling and prediction, it is beneficial to reduce the number of parameters and link the CP's properties directly to the strength and duration of a rain event. For this purpose, we here empirically derive a scaling of CP properties in terms of the potential energy of the one-time (i.e., discontinuous) initial cold air anomaly. We argue that despite the simplifications, these results can be used to understand how CP dynamics scales with the size and intensity of rain events.

We then study the triggering of convection events by CPs, focusing on whether new events are more often triggered at a single front or where multiple fronts collide. We examine this distinction from a dynamic perspective, considering the likelihood of triggering new convection to increase with the strength and height of updrafts that are generated at the gust front of a single CP or at collision lines where multiple CPs meet. In this context we assume the likelihood of new convection to monotonically increase with the strength of the vertical updrafts that are generated by the horizontal convergence ahead of the CP head and the time-integrated mass flux at a given location. A similar argument has been used by Feng et al. (2015), who show that at locations where two or more CPs collide, updraft strength tends to be increased.

The setup of the large-eddy simulations is described in Sec. 2. Results are presented in Sec. 3 and 4 for single and multi-CP effects and we end with a discussion (Sec. 5), which relates the results to the more complex, moist convection in more realistic settings.

2 Large-Eddy Simulations

Simulation setup. The simulations are run using the large-eddy simulation (LES) code PyCLES (Pressel et al., 2015) to solve the anelastic equations for momentum and entropy. Sub-grid scale (SGS) diffusion is added using the Smagorinsky scheme (Smagorinsky, 1963). The resolution is isotropic with $\Delta x = \Delta y = \Delta z = 25$—100m, domain size $L_{x,y} = 20$—80km horizontally and $L_z = 12$km vertically. We employ periodic lateral boundary conditions. Turbulent fluctuations are initialized by adding weak noise in potential temperature θ of amplitude $\theta' = 0.05$K in all levels below $z = z^* + 2 \cdot \Delta z$, where z^* is the height of the initial cold air anomaly.

2.1 Cold pool initialization

The CPs are initialized by an initial 'mountain' of cold air of height z^* and circular base of radius r^* at the lowest level (Equation A2, Fig. A1). To lower numerical errors, a transition layer of thickness $\delta = 200\,\mathrm{m}$ is applied, in which the temperature anomaly smoothly decreases from $\theta = \theta_0 + \theta'$ to $\theta = \theta_0$. The temperature anomalies θ' are chosen commensurate with observations of deep tropical convection over the ocean, with $\theta' = -2\,\mathrm{K}$ to $-5\,\mathrm{K}$ (Feng et al., 2015; Zuidema et al., 2017). The parameters for amplitude and geometry of the θ' are chosen such that after the initial spin-up time, the CP properties resemble those observed in unorganised tropical convection over the ocean (Feng et al., 2015; Zuidema et al., 2017), where CPs are weaker than in (organised) continental convection.

2.2 Surrounding environment

Neutral Stratification. The CPs spread into a calm, neutrally stratified environment with $\theta_0 = 300$K (Fig. 2), where all velocities are initially set to zero. No surface fluxes are applied, leading to extended life time of the CPs due to decreased dissipation near the surface. As motivated by Droegemeier and Wilhelmson (1987), such a highly idealized setup allows to isolate the effects of CPs on the environment without the obscuring effects from wind shear and gravity waves or the collision with existing circulation patterns from previous convection events. To test the results of the CP collisions in a more realistic environment, an additional set of experiments is conducted in a stably stratified atmosphere.

Stable Stratification. Atmospheric soundings usually show a stable stratification above the boundary layer top. To test the effect of stratification on the updrafts generated at CP gust fronts and during CP collisions, we compare simulations with neutral and weakly stable stratification at $z > 1000$m, adopting the conditions used in Grant and van den Heever (2018) to a dry atmosphere. The stable case is characterized by a constant Brunt-Väisälla frequency of $N_v^2 = \frac{g}{\theta}\frac{\partial\theta}{\partial z} = 5 \cdot 10^{-5}\mathrm{s}^{-2}$. This induces gravity waves atop the CP centre, at an oscillation period $\tau \sim N_v^{-1} \approx 140\,\mathrm{s}$.

2.3 Cold Pool Collisions

To study CP collisions, the simulations are initialised with two or three identical CPs, with CP centers separated by a distance $d = 10$, 15, and 20km. In the three-CP collision, d corresponds to the side length of the equilateral triangle with CPs initialised at all three corners (Fig. 6). The values of d are in line with typical distances between the centres of convective events in radiative-convective equilibrium simulations (Nissen & Haerter, 2020).

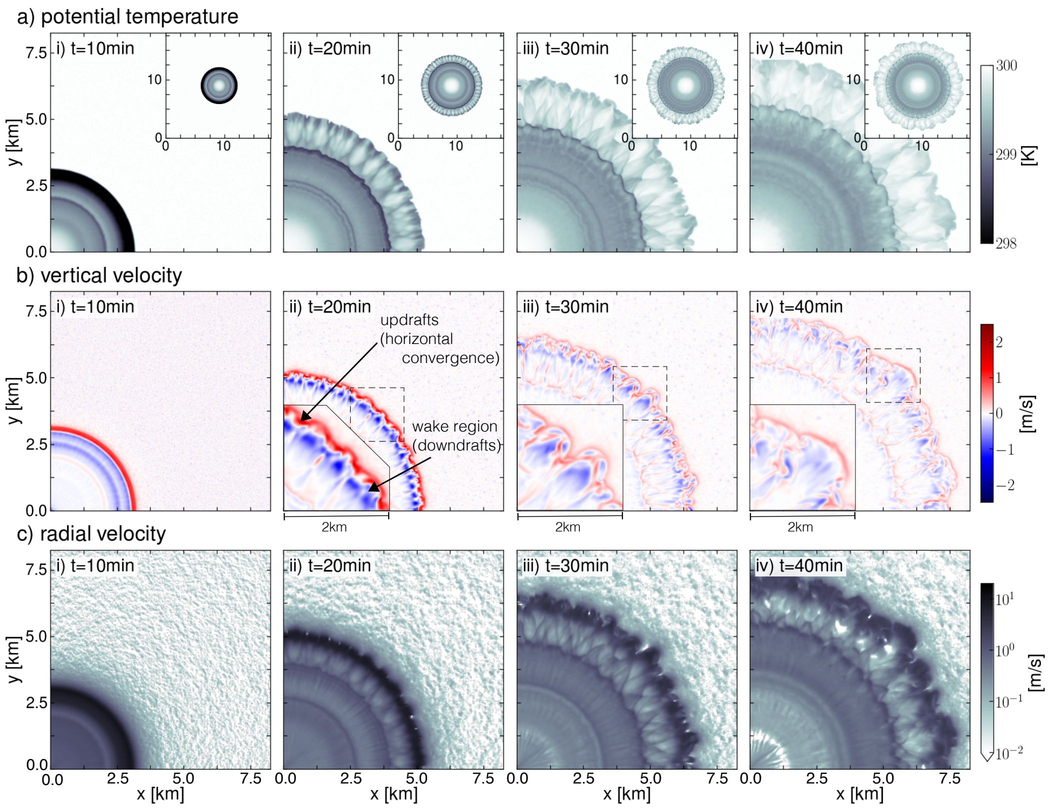

Figure 2. Internal cold pool structure. Horizontal cross sections of temperature and velocity in the lowest model level at various times after initialization (*see* the labels within the panels). The temperature anomaly was initialised as $\theta' = -3\text{K}$ and the geometry parameters $r^* = z^* = 1\text{km}$ (grid spacing $\Delta x = 25\text{m}$). **a)** potential temperature; **c)** vertical velocity showing updrafts (red) and downdrafts (blue); and **c)** radial velocity. Insets in a) show an overview of the total CP.

3 Results Single Cold Pool

3.1 Cold pool structure

After initialisation, the cold air 'mountain' collapses and spreads isotropically along the surface, forming the CP (Fig. 2). During the first 10–15 min, the CP retains its almost perfect circular symmetry, where deviations from the azimuthal mean are small both in the temperature and velocity fields (Fig. 2i).

During the collapse of the cold air 'mountain', the horizontal temperature gradient induces baroclinic generation of a vortex sheet along the lateral boundary of the temperature anomaly, which finally rolls up into a vortex ring that forms the clearly visible CP head (Fig. 3d) (Droegemeier & Wilhelmson, 1987; Markowski & Richardson, 2010; Rooney, 2018). While spreading, the CP head becomes fairly detached from the shallow CP interior and maintains a colder and deeper temperature anomaly (Fig. 3a).

The vortical circulation leads to a dipole-structure in vertical velocities w with strong updrafts ahead of and downdrafts behind the CP head in the wake (Figs. 2b, 3b). In this downdraft region warm environmental air is entrained into the CP head, boosting the CP's dissipation. This mixing together with surface fluxes accelerates the CP dis-

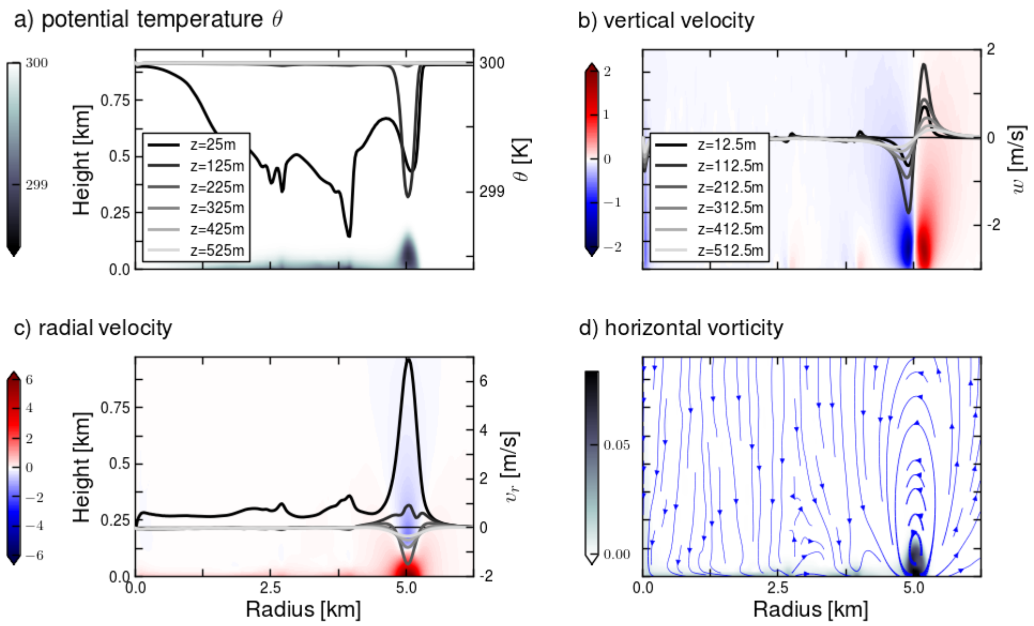

Figure 3. Thermodynamic and dynamic signature of a spreading cold pool. a) z-r contourplot and cross sections of azimuthally averaged potential temperature θ, where the cross sections show increasing levels of z (*see* legend) 20min after CP initialisation (LES parameters analogous to Fig. 2). **b)**, analogous to a), but for vertical velocity w; **c)** analogous to (a), but for radial velocity v_r; **d)** similar, but showing vorticity projected onto the radial vector, with superimposed streamlines of v_r and w.

sipation. Ahead of the CP head, the vortex ring and the spreading of the CP form a band of convergence of the horizontal velocity (Figs. 2c, 3c).

The profiles of temperature and velocity (Fig. 3a–c) compare well to previous numerical studies, both in idealised (Droegemeier & Wilhelmson, 1987; Romps & Jeevanjee, 2016) and more comprehensive setups (Drager & van den Heever, 2017; Fournier & Haerter, 2019). The main difference to the latter study is, that the CP head there is less detached from the CP interior due to the more continuous forcing from rain events with a finite life time.

At a more mature stage, the vortex ring develops along-front instabilities that break the symmetry of the vortex ring (CP head) by dividing it into smaller cells typically measuring 500−1000m in diameter (Fig. 2, insets). These so-called 'lobe-and-cleft' instabilities occur as the CP head overruns lighter air that is trapped near the surface, leading to hydrodynamic linear instabilities that have been studied both in theory and laboratory experiments of gravity currents (J. E. Simpson, 1972; Markowski & Richardson, 2010; Wakimoto, 2001; Härtel et al., 2000). As shown in Section 3.2, these instabilities have a crucial effect on the spreading velocity of the CP (Fig. 5). It remains an open question, to which extent 'lobe-and-cleft' instabilities play a role in observations and comprehensive cloud-resolving simulations, where CPs also spread into the environment not as a homogeneous front, but by protruding edges. In the interior of these edges (lobes), a circulation tangential to the CP front develops, which is reflected in an increased tangential velocity component of alternating direction. This alternating pattern creates regions of enhanced horizontal convergence and thus vertical updrafts along the CP edge, where the triggering of new convective events may be enhanced.

Since we are interested in the dynamic forcing by CPs, namely the location and strength of generated updrafts, we define the *CP radius* R as the distance between the CP center ($r = 0$) and the location of the maximum low-level convergence of horizontal wind

$$R = \max_r(\vec{\nabla}_h \cdot \vec{v}_h), \tag{1}$$

which is co-located with the maximum of the vertical updrafts $\max_r(w(r, \phi))$. This radius R and the corresponding propagation speed of the CP $U \equiv dR/dt$ are determined using a tracer method introduced in Henneberg et al. (2019). The CPs spread to radii of approximately 10 km within an hour, which is in line with other numerical and observational studies (Tompkins, 2001a; Feng et al., 2015; Romps & Jeevanjee, 2016).

Due to the vortical circulation in the CP head this method only allows to define the CP boundary at the lowest model levels ($z \leq 200 - 300$m). At higher levels, the radial velocity becomes weaker until it reverses direction at the upper boundary of the CP head, resulting in weaker and more noisy horizontal convergence. For this reason, we define the *CP height* based on the thermodynamic signature, determining for each column the highest level where the potential temperature deviates by more than a small threshold $\epsilon = 0.1$K from the background temperature $\theta_0(z)$

$$H(x, y) = \max_z \left(|\theta_{\mathrm{CP}}(x, y, z) - \theta_0(z)| < \epsilon\right). \tag{2}$$

Such a simple method is found sufficient in this idealised setup where the temperature is very homogeneous in the environment.

3.2 Scaling of cold pool properties with initial potential energy

This section considers the hypothesis that key CP properties, such as CP propagation speed and the strength of the generated updrafts at the CP gust front, are insensitive to the exact shape and temperature anomaly of the initial configuration, but are solely determined by the initial potential energy (termed PE). This notion builds on early theoretical studies by Benjamin (1968) and Rotunno et al. (1988) and adds detail to the sensitivity study on outflow morphology and structure by Droegemeier and Wilhelmson (1987), by showing that the parameter space of at least three variables (magnitude, depth and vertical shape of the cooled volume) can be collapsed to a single dimension — namely that of PE — a quantity that can be studied in the context of energy budgets.

In our simple dry setup with neutral background stratification, PE depends on the initial temperature anomaly θ' and the volume of the initial 'mountain' — in turn a function of the geometry parameters for the height and radius of the anomaly, termed z^* and r^*, respectively. As an integral over the specified volume (Eq. A2), PE can be computed as

$$PE \quad = g\tfrac{\theta'}{\theta_0} \int \mathrm{d}V \, \rho_d(z) \cdot z \approx g\tfrac{\theta'}{\theta_0} \rho_0 \int \mathrm{d}V \, z \propto \theta'(r^* z^*)^2, \tag{3}$$

where $\rho_d(z) \approx \rho_0 \approx 1\mathrm{kg\,m^{-3}}$ is the density of dry air (*compare* Appendix A for details).

First, we run experiments where PE is held constant at a reference value $\mathrm{PE}_0 \approx 4.4{\cdot}10^7$kJ, whereas r^*, z^* and the initial temperature anomaly θ' are varied. PE_0 corresponds to a CP with initial temperature anomaly $\theta'_0 = 3$K and $r^*_0 = z^*_0 = 1$km. These experiments allow us to test whether the initial shape of the CP impacts on its dynamics. Second, PE is varied, and the resulting scaling of CP properties studied — mimicking changes in precipitation intensity and resulting CP strength. Such intensity changes can occur within the diurnal cycle of precipitation, where intensifying precipitation cells might release increasingly more energy (Haerter et al., 2017, 2020).

Sensitivity to geometry and temperature anomaly. First, the temperature anomaly is varied from as $\theta' \in \{-2, -3, -4\}$ K, whereas the geometry is adjusted only as much as is necessary to keep the PE constant (Fig. 4a–d). Second, $\theta' = -3$K is held constant whereas the geometry is varied from a narrow and tall to a broad and shallow mountain (Fig. 4e–h).

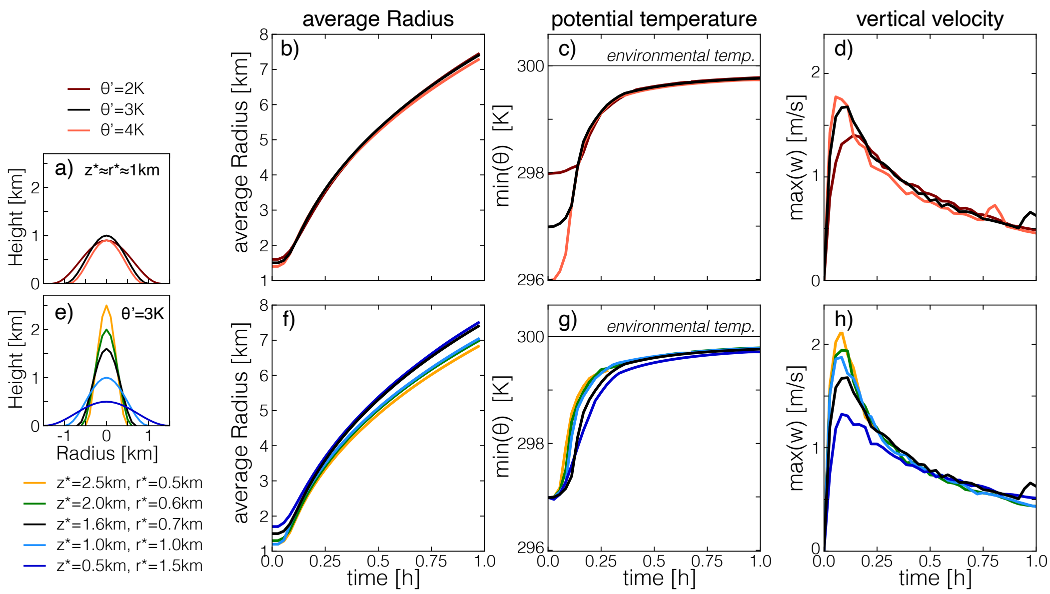

Figure 4. Timeseries of CP properties when holding potential energy fixed. a) schematic of CP geometry and temperature, when systematically modifying the temperature anomaly $\theta' \in \{-2, -3, -4\}$ K (as shown in the legend), but approximately maintaining the ratio of the geometry parameters $(r^*, z^*) = \{(1.3\,\text{km}, 0.9\,\text{km}), (1.\,\text{km}, 1.\,\text{km}), (.9\,\text{km}, .9\,\text{km})\}$ ($\Delta x = 50\,\text{m}$, $L_x = 40\,\text{km}$), **b)** azimuthally averaged CP radius vs. time after initiation, **c)** analogous, but for domain minimum potential temperature, **d)** analogous, but for maximum vertical velocity in the updrafts ahead of the CP, **e)** analogous to panel a, but now systematically varying the ratio of z^* and r^* (modifying the geometry, see legend) at fixed $\theta' = 3$ K, again maintaining $PE = PE_0$. **f–h)** analogous to panels b–d, but for the initial conditions shown in panel e.

The resulting CPs show very similar properties during their life cycles. The timeseries (Fig. 4) represent mean, minimum or maximum values of azimuthally averaged quantities: the average radius R (Eq. 1); the minimum potential temperature as a measure of CP dissipation, defined as $\theta_{\text{min}}(t) = \min_{r,z}\left[\int d\phi\,\theta(r,\phi,z;t)\right]$; and the maximum vertical velocity $w_{\text{max}}(t) = \max_{r,z}\left[\int d\phi\, w(r,\phi,z;t)\right]$. It has been verified that the points of minimum potential temperature and maximum vertical velocity are measured within or in near proximity ahead of the CP head respectively. The timeseries differ mostly at the initial formation of the density current ($t \leq 15$ mins), but converge soon thereafter. Hence, after a spin-up time between initialization and density-current formation, the simulations are rather insensitive to the geometry and temperature anomaly of the initial configuration, and are largely determined by the initial PE.

Scaling with initial potential energy. All CPs are now initialized by $\theta' = -5$ K and $z^* = 1$ km, whereas r^* is varied to scale the CPs' initial PE (Figs. 5a, b). Resolution is $\Delta x = 50$ m and domain size is $L_x = 80$ km. The initial cooling can be thought of as generated by rain of varying intensity that evaporates uniformly within the sub-cloud air column of height $z^* = 1$ km below a cloud of area $A = \pi r_0^{*2} \approx 3\,\text{km}^2$ (Fig. 5d). Corresponding rain intensities from rain events of duration $\tau = 30$ min and evaporation rates of $\eta = 20\%$ (Worden et al., 2007) are shown in Fig. 5c (*compare:* calculation in Appendix B).

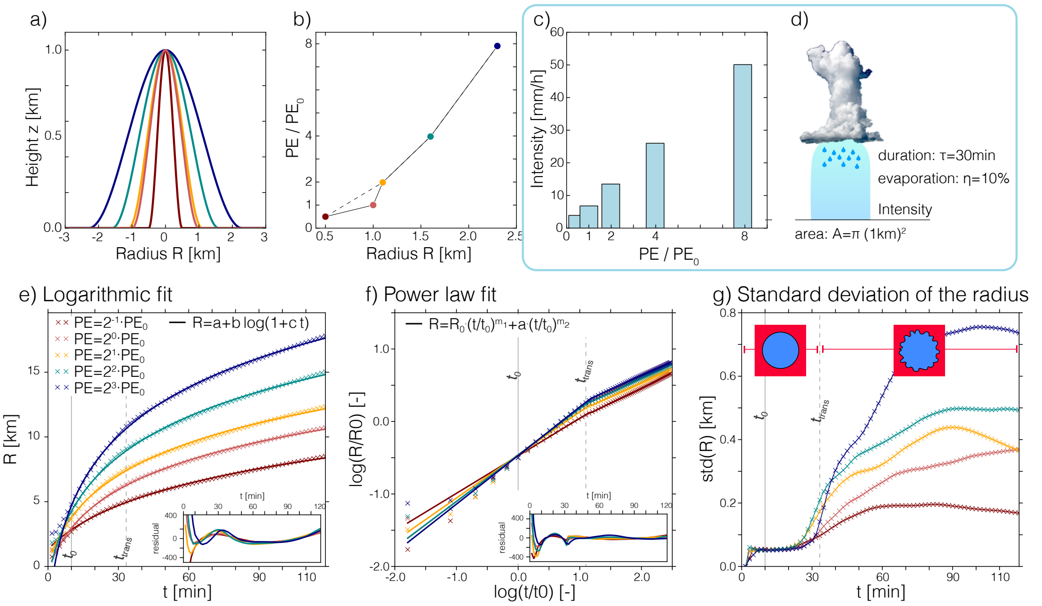

Figure 5. **Scaling of cold pool radius with potential energy. a), b)** Initial geometry and corresponding PE. Symbol colors in (b) correspond to those of the different shapes in (a); **c)** the relation of PE to precipitation intensity under simplifying assumptions **d)** sketch and values of underlying assumptions for c).**e)** Timeseries of the CP radius R for increasing PE (configurations as in a) ("×" symbols). Solid lines are logarithmic fits using $R = a + b\log(1 + ct)$ (Romps & Jeevanjee, 2016), and the solid and dashed vertical black lines indicate t_0, to define $R_0 = r(t = t_0)$, and t_{trans}. **f)** Log-log plot of R vs. t ("×" symbols) with best fits for power-law scaling from Eq. 4 (solid lines) (note that $\log(x)$ denotes the natural logarithm); **g)** Timeseries of the standard deviation $\sigma(R)$ of the tracer radius, showing the transition from the axisymmetric CP state (small, approx. constant $\sigma(R)$) to the mature CP whose head is dominated by 'lobe-and-cleft' instabilities (*compare*: Fig. 2).

For all initial values of potential energy, CP expansion monotonically slows down, which has been described in previous studies. Romps and Jeevanjee (2016) approximated the decrease by a logarithmic dependence of radius on time, that is, $R(t) = R_0 + b\log(1 + c(t - t_0))$. Fitting the three parameters R_0, b, c to our simulation data indeed yields a visually acceptable fit within the time range considered (Fig. 5e). When examining the residuals (Fig. 5e, inset), systematic oscillations are however visible for all cases. When plotting the data using double-logarithmic axis scaling (Fig. 5f), it becomes clear, that a transition between two power laws, each of the form

$$R(t) = R_0\,(t/t_0)^m \tag{4}$$

but with a change in exponent m at a time t_{trans}, may also be appropriate. The reference value R_0 is thereby a function of PE and t_0, i.e.,

$$R_0(\text{PE}) = R(t_0, \text{PE}), \tag{5}$$

where the choice of reference potential energy PE_0 is arbitrary and $t_0 = 10\,\text{min}$ is chosen as the spin-up time. The discontinuous slope in the log-log plot (Fig. 5f) hence indicates a separation of the CP lifecycle into two dynamical regimes between which the power-law exponent m changes. The transition occurs near $t_{\mathrm{trans}} \approx 30\,\mathrm{min}$ and we attribute it to a dynamical transition from an axi-symmetric state to one where 'lobe-and-cleft' instabilities dominate the CP head (*compare*: Fig. 2). This interpretation is verified by the standard deviation of the CP radius, which experiences a strong increase at the transition time (Fig. 5g). This transition time appears to be independent of the potential energy, whereas the thermal nature of the instability suggests that it may vary with the initial temperature anomaly θ' as discussed in Sec. 3.1.

Logarithmic fit	$\mathbf{r}^*$ $[km]$	$\boldsymbol{\delta R}$ [m]	$\mathbf{R_0}$ $[m]$	$\mathbf{b}$ $[m]$	$\mathbf{c}$ $[10^{-3}\,s^{-1}]$
$\hat{R}(t) = a + b\,\log(1+ct)$	.5	8.	2835.	3573.	0.6
	1.0	7.9	2971.	3871.	1.0
	1.1	12.0	3803.	4248.	0.9
	1.6	12.2	4272.	5084.	1.1
	2.3	10.5	4699.	5811.	1.3

Power-law fit	$\mathbf{r}^*$ $[km]$	$\boldsymbol{\delta R}$ [m]	$\log\,\mathbf{a_1}$ $[-]$	$\mathbf{m_1}$ $[-]$	$\log\,\mathbf{a_2}$ $[-]$	$\mathbf{m_2}$ $[-]$
$\hat{R}(t)/R_0 = a_i\,(t/t_0)^{m_i}$	.5	3.5	0.0	0.52	0.1	0.42
$i = 0$, for $t < t_{\mathrm{trans}}$	1.0	3.3	0.0	0.64	0.3	0.41
$i = 1$, for $t \geq t_{\mathrm{trans}}$	1.1	5.0	0.0	0.59	0.3	0.39
	1.6	5.0	0.0	0.64	0.3	0.39
	2.3	5.4	0.0	0.67	0.4	0.38

Table 1. Fitting parameters and errors for the mean CP radius as a function of time and initial potential energy. The radius $\hat{R}(t)$. Here, $t \in \{t_0,\, t_0 \;\; + \;\; 100, \ldots, 7100\,\}\,s$, with the spin-up time $t_0 = 10\,\mathrm{min}$ and $n_t = 65$ the total number of time steps. The transition time is chosen at $t_{\mathrm{trans}} = 2000\,\mathrm{s}$. The mean square-root error is computed as $\delta R = \frac{1}{n_t}\sqrt{\sum_{i=1}^{n_t}\left(\hat{R}_i - R_i\right)^2}$, where $\hat{R}_i = \hat{R}(t_i)$ is the estimated radius (from power-law or logarithmic fit, respectively) and $R_i = R(t_i)$ the measured CP mean radius at time t_i.

The two scaling functions are compared in terms of their 'goodness of fit,' considering the number of parameters, root-mean-square deviation δR and their physical explanatory power, i.e., how well they allow to separate the dependence on time from the dependence on PE. If for the power-law fit

$$\hat{R}(t)/R_0 \quad = a_i\,(t/t_0)^{m_i}, \qquad \begin{aligned} &i = 1 \text{ for } t_0 \leq t < t_{\mathrm{trans}}, \\ &i = 2 \text{ for } t \geq t_{\mathrm{trans}}, \end{aligned}$$

a fixed transition time t_{trans} is chosen and R is re-scaled by R_0, the axis intercept a_1 becomes zero (Table 1). Thus both fitted functions, logarithmic and power-law, are determined by three parameters, which renders a comparison with respect to fitting errors valid. The power-law fit outperforms the logarithmic fit both in terms of lower systematic error (compare: Fig. 5d,e insets) and lower least-square error δR (Table 1). Finally, for the logarithmic scaling, the optimal fitting parameters differ quite strongly for varying PE, whereas power-law exponents are approximately constant (Table 1): $m_1 \approx 0.5$–0.6, $m_2 \approx 0.4$. This gives the power-law fit a more universal character.

4 Results Cold Pool Collisions

To simulate the collisions, we initialize two (*2CP*) or three (*3CP*) identical CPs separated by distances of $d = 10$, 12, and $15\,\mathrm{km}$ (Sec. 2). The updrafts generated and the corresponding mass fluxes are compared to an otherwise identical single CP (*1CP*) which spreads unrestrictedly. All CPs are initialized with $\theta' = 5\,\mathrm{K}$, $z^* = 1\,\mathrm{km}$ and $r^* = 1.1\,\mathrm{km}$.

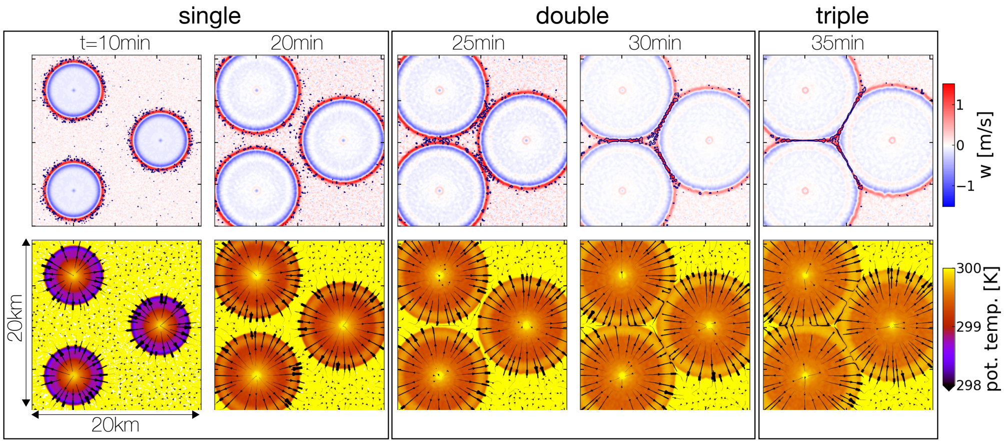

Figure 6. Simulated three-CP collisions. (top) Vertical velocity at the lowest model level $w(z = 50\,\mathrm{m})$ with contours depicting vertical velocity at higher level ($w(z = 550\,\mathrm{m}) \geq 0.5\,\mathrm{m/s}$) indicating the updrafts triggered in the CP collisions (fluctuations at early times are forced by the initial temperature perturbations). (bottom) Potential temperature with streamlines of the horizontal wind field, both at the lowest model level ($z = 25\,\mathrm{m}$). Data from *3CP* simulation with $d = 12\,\mathrm{km}$ at $t = 10$, 20, 25, 30, and 35 min.

Notably, the CPs have a very short "communication distance", that is, they affect their environment and other CPs only within a very short distance beyond their leading edge, as visible in the very weak horizontal and vertical velocities outside the temperature anomaly (Fig. 6). We thus define a CP collision as the instance when the CPs' gust fronts touch, defining the times of 2-CP collision ($t_{2\mathrm{CP}}$) and 3-CP collision ($t_{3\mathrm{CP}}$); c.f. Table C1. The collisions are delayed by approximately 10 min when d is increased by 5 km; indicating that the CPs spread at an average speed of 8 m/s.

Updraft generation. Figure 7 shows the maximum values of vertical velocity w (upper row) and minimum values of potential temperature (lower row) at each model level. During the first 10–30min ($t_0 \leq t < t_{2\mathrm{CP}}$), the CPs of the multi-CP simulations (*2CP*, *3CP*) do not measurably affect each other. This results in equivalent CP properties for all simulations *1CP*, *2CP*, *3CP*, and all separation distances d (Fig. 7b, f). The strongest updrafts are generated right ahead of the CP head, extending up to a height of roughly 1000 m, with strongest vertical velocities ($w \approx 2\,\mathrm{m/s}$) at the lowest model levels (100–300 m). The strength of these updrafts remains roughly constant while the CPs spread.

When the CPs collide in pairs of two ($t = t_{2\mathrm{CP}}$), they form collision lines where the ambient air is displaced both vertically and horizontally along the collision lines, as the flow is constraint to these two degrees of freedom. This creates updrafts that are both faster and reach greater heights: the vertical velocity is strongly increased in the lower boundary layer ($z < 600$m) (Figs. 6, 7c) and the CP height is nearly doubled to $H_{\mathrm{max}} \approx 700 - 800\,\mathrm{m}$ (Fig. 7g). Notably, the maximum velocity for *2CP* is more than twice as large as for *1CP*. This factor indicates that the updrafts generated in CP collisions cannot simply be described as superpositions of the single CP updrafts, and that horizontal kinetic energy may be transformed into vertical motion during the collisions. This non-linearity may be enhanced by the superposition of the vortical circulation in the two CP heads (Cafaro & Rooney, 2018).

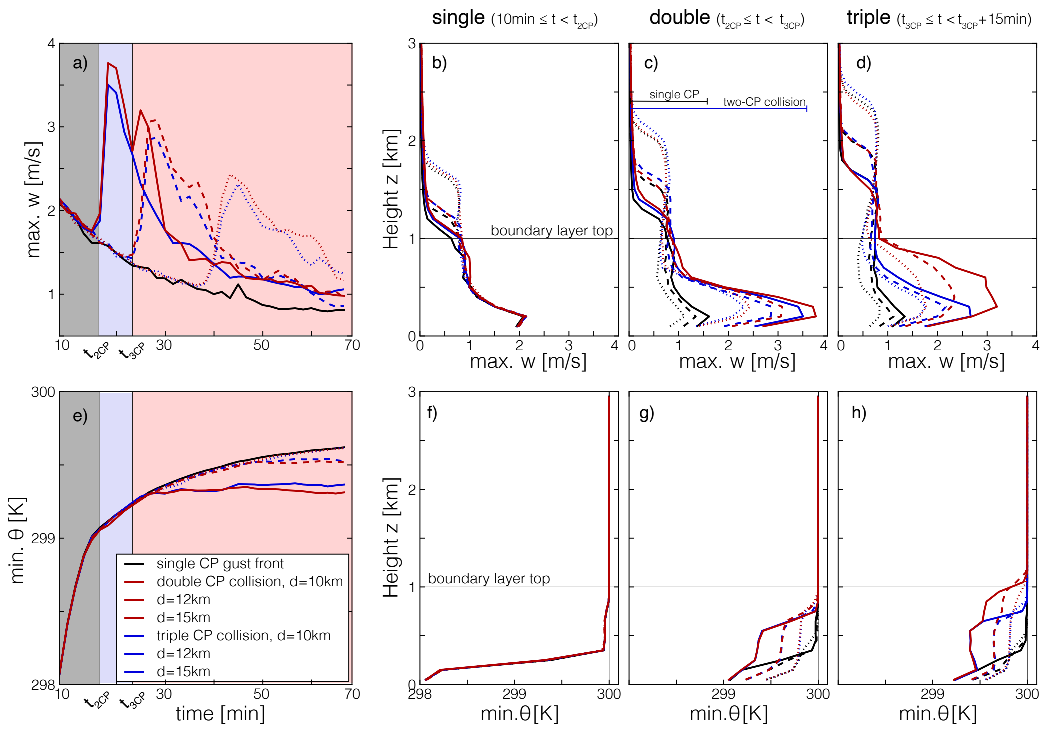

Figure 7. Updraft speed and CP height in collisions. a) Timeseries of domain maximum values of vertical velocity w for the *1CP* (black), *2CP* (blue) and *3CP* (red) simulations with neutral background stratification. Line styles indicate different initial CP separation of $d = 10$km (solid line), 12km (dashed line), and 15km (dotted line); background color-shadings refer to the time windows of undisturbed CPs (grey), two-CP collision (light blue) and three-CP collision (light red). **b)-d)** Maximum values of vertical velocity w at each model level during the time window of (b) the single CP spreading, (c) two-CP collision and (d) three-CP collision, **e)–h)** analogous to a)–d), but for minimum values of potential temperature θ.

As the CPs continue to spread, the collision lines grow until in *3CP* they eventually meet at the center of the domain, forming a three-CP collision ($t = t_{3\mathrm{CP}}$). The warm ambient air, enclosed by the CPs, as well as the colder CP air is then forced upwards by the low-level convergence. The vertical velocity peaks in a locally very confined area around the collision point (Fig. 6 at $t = 35$ min). This three-CP collision generates enhanced vertical velocities in the middle boundary layer ($z = 400 - 800$m), with an increase from 1–1.5 m/s to 2.5–3 m/s (*compare* red lines in Fig. 7d). In the lower boundary layer, these velocities are however lower than in the earlier two-CP collision.

The enhanced velocities above the boundary layer ($z > 1000$ m) are an artefact of the neutrally stratified atmosphere that allows any positive buoyancy perturbation to rise indefinitely. In more realistic atmospheres with stable stratification above the boundary layer, these updrafts are capped at the top of the boundary layer (*see* discussion below and Fig. C1).

Upward transport of cold pool and surface air. In the triggering of convection not only the strength but also the height of the updrafts is important, both from a dynamic and thermodynamic perspective. The kinetic energy from strong updrafts at higher levels can help overcome stable layers that cap a boundary layer (Fig. 9, (Grandpeix & Lafore, 2010)). From a thermodynamic perspective, convection is favoured by a (gradual) moist-

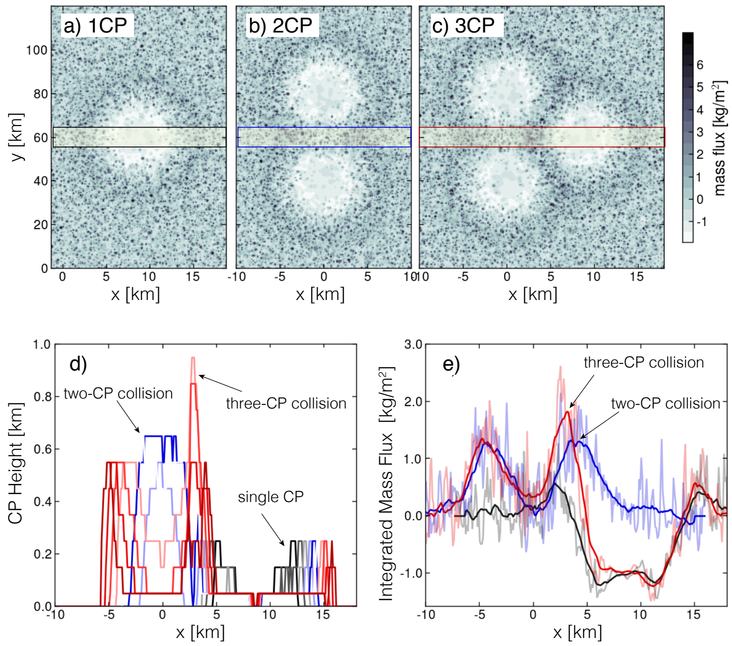

Figure 8. Cold pool height and accumulated vertical mass flux. a) Horizontal cross section of the accumulated vertical mass flux at $z = 1\,\mathrm{km}$ for *1CP*, integrated from $t = 10\,\mathrm{min}$ after initialisation to $t_{3\mathrm{CP}} + 10\,\mathrm{min}$.The yellow box indicates the band of width $2\,\mathrm{km}$ along which MF is averaged for e); **b), c)** as a), but for the *2CP* and *3CP* simulations. The same integration time window is used for each simulations, to ensure meaningful comparison. **d)** CP height in *3CP* along the box indicated in c) during the single CP phase (gray to black), two-CP phase ($t_0 \le t < t_{2\mathrm{CP}}$; blue shadings), and three-CP phase ($t_{2\mathrm{CP}} \le t < t_{3\mathrm{CP}}$; red shadings) (initial separation $d = 10\mathrm{km}$). **e)** Accumulated mass flux at $z = 1\,\mathrm{km}$, spatially averaged over a band of $2\,\mathrm{km}$ width along the CP collision line, as indicated by the yellow shaded box in a-c from *1CP* simulation (black),*2CP* simulation (blue), and *3CP* simulation (red).

ening of the free-troposphere air when moist near-surface and boundary layer air is lifted above the lifting condensation level (LCL). Numerical and observational studies have identified a (gradual) pre-moistening of the mid-troposphere (between 2 and $4\,\mathrm{km}$) as an important process preceding the onset of heavy rainfall events and the transition from shallow to deep convection (Zhang & Klein, 2010). Specifically in the absence of large-scale advection of moist air masses, this moistening seems to be provided by local shallow convection.CPs may play an important role in accelerating this process by concentrating the moisture in the boundary layer, thereby clustering and widening the shallow convective clouds (Seifert & Heus, 2013; Schlemmer & Hohenegger, 2014; Kurowski et al., 2018). Little consideration however is usually given to the role of CPs in enhancing and spatially concentrating the moisture in the lower troposphere by increased mass flux along CP gust fronts. During CP collisions, these fronts become stationary and thus increase the moisture in a confined area for an extended period of time (Fuglestvedt & Haerter, n.d.).

As a proxy for the moisture flux, we consider the accumulated vertical mass flux through the top of the boundary layer (here assumed to be at $z_{\mathrm{BL}} = 1\,\mathrm{km}$)

$$\mathrm{MF}(x, y, z_{\mathrm{BL}}) = \int_{t_0}^{t_1} \mathrm{d}t\, \rho(t, x, y, z_{\mathrm{BL}})\, w(t, x, y, z_{\mathrm{BL}}),$$

where ρ is the density of air, $t_0 = 10\,\text{min}$ is the spin-up time and $t_1 = t_{3\text{CP}} + 15\,\text{min}$ (*compare* Fig. 8a–c).This mass flux is clearly enhanced along the two-CP collision lines and peaks above the three-CP collision point (Fig. 8d). This enhancement can be understood as a result of the combining effects of increased vertical velocities and the stationary location of the updraft fronts, which allows the updrafts to increase the moisture within a confined area over longer time.

Additionally, the CP height serves as an estimate of the height to which the near-surface air is transported (Fig. 8c). Throughout the single-CP time window ($t_0 \leq t < t_{2\text{CP}}$), the CP height remains roughly constant at about 200m (Fig. 8d, black curves). During the two-CP collision, the cold air is pushed to above 600 m (blue curves). Finally, in the three-CP collision, the air is pushed close to the boundary layer top at 1 km (red curves). By using passive tracers, initialized at the lowest model level, we verified that the CP height as measured above indeed gives a lower bound on the lifting level of near-surface air.

Stable Atmosphere. Similar analyses were conducted in simulations with stably stratified atmosphere (at $z \geq 1000\,\text{m}$). The CPs expand at slightly decreased speed, resulting in later collision times (Table C1). This reflects theoretical findings of slower gravity current propagation speeds in channels of decreased depth (Benjamin (1968)). In the boundary layer, the collisions lead to very similar results (Fig. C1), differing only in that updrafts are somewhat shallower in the stable case ($z < 700\,\text{m}$ vs. $z < 900\,\text{m}$). Above the boundary layer ($z \geq 1000\,\text{m}$), the simulations differ strongly, as in the stable case the initial collapse of the cold air anomaly generates gravity waves that generate strong vertical velocities aloft the boundary layer. These waves are reinforced when the CPs collide and enhanced the mass flux locally.

5 Discussion and Conclusion

Our LES experiments represent highly simplified CP dynamics. This allows to isolate the dynamic effects of CPs from unsystematic perturbations in the CPs' surroundings, such as pre-existing wind shear or variations in temperature and moisture. By removing such perturbations we can probe, how CP properties scale with the intensity and size of the rain cell that caused the CP's initial potential energy (PE) and compare updraft strength and massflux that are generated in collisions of two and three CPs.

Insensitivity to initial cold pool geometry.
To a good approximation, key dynamic features, such as CP propagation speed and the strength of convergence and updrafts ahead of the CP head, are insensitive to the geometry and temperature of the initial cold air anomaly, as long as the CP's potential energy is kept constant. This initial PE combines the spatial and (dry) thermodynamic parameters of CP initialisation, which reduces the space of scaling parameters (Droegemeier & Wilhelmson, 1987) to a single extensive and conserved variable. Some sensitivity to the geometry of the initial perturbation can be observed in the CP volume and maximum vorticity in the CP head, resonating with Droegemeier and Wilhelmson (1987). From a modeling perspective, the detected insensitivity to the initial geometry allows to generalise our results and compare them to studies that use different initialisation configurations, such as cold bubbles that are released above the surface (Rooney, 2015; Grant & van den Heever, 2016).

In our simplified setup, moisture and microphysics are neglected. However, since PE is an extensive variable, it can be related to the amount of rain that is required to evaporate to cool the sub-cloud air column through latent heat uptake (*compare* Fig. 5). In estimating how much rain has to evaporate to generate the CP's potential energy, we approximate the entire rain volume to fall instantaneously, hence assuming that dissipation of potential energy is slow compared to the lifetime of the rain event. Under these assumptions, the sensitivity experiments presented in Sec. 3.2 (Fig. 4) indicate that precipitation intensity and cell size combined determine the strength of CPs. The scaling of CP expansion with PE furthermore may assist a better understanding of the kinetics and internal vortical circulation of CPs, which play a crucial role in the mechanic forcing during CP collisions (Cafaro & Rooney, 2018) and are important factors for CP dissipation (Romps & Jeevanjee, 2016; Grant & van den Heever, 2016, 2018; Rooney, 2018).

The steady-state CP propagation speed U for inviscid and incompressible gravity currents has been expressed as (Benjamin, 1968; von Karman, 1940)

$$U = \sqrt{2gH\frac{\rho'}{\rho}} \approx f(\mathrm{PE}_d)\,. \tag{6}$$

Here, the potential energy density can be approximated as $\mathrm{PE}_d \approx g\rho' H$, allowing to relate this expression to our scaling. However, such a steady-state solution requires a continuous forcing of the gravity current, provided by a constantly cooling source of PE in inflow experiments, and does not explain the decreasing CP propagation velocity with time. The power-law scaling we propose (Eq. 4) is more in line with the dynamics derived from similarity theory ($R \sim t^{1/2}$; Rooney (2015)) or vorticity conservation ($R \sim t^{2/3}$; Rooney (2018)). The latter assumes that the vortical circulation in the CP head (*compare* Fig. 3) is maintained and drives the CP propagation through its interaction with the surface. This seems to be a good prediction for the strong CPs ($r^* > 1000\,\mathrm{m}$) before the observed dynamic transition ($t < t_{\mathrm{trans}}$). We interpret the "kink" in scaling at the transition as an abrupt re-partitioning of kinetic energy from a predominantly radial component to an additional strong azimuthal contribution by the onset of 'lobe-and-cleft' instabilities. This could be seen as the activation of additional degrees of freedom at $t = t_{trans}$. We speculate that the lower exponent after the transition ($m_2 \approx 0.4 < 2/3$) originates from the quick decay of vorticity after the onset of instabilities.

Importance of cold pool collisions.
Our results on CP collisions (Sec. 4) can be summarised as follows: during two-CP collisions, strongest mid-boundary layer updrafts are generated where the two CPs meet. These updrafts are somewhat amplified if a third CP is present in the vicinity. During a three-CP collision, low-boundary layer updrafts are slightly weaker, most likely due to CP dissipation during their life cycle. However, updrafts in the upper boundary layer ($400-900\,\mathrm{m}$) are enhanced where the three CPs meet and cold CP air is forced much higher up ($1000\,\mathrm{m}$). This implies, that moist near-surface air is mechanically lifted above the boundary layer and the lifting condensation level (LCL), where it either directly initiates a new convective event or contributes to pre-moistening as a crucial precursor for deep convection (Zhang & Klein, 2010; Kurowski et al., 2018). Accumulated vertical mass flux is a useful proxy for vertical moisture transport, combining updraft height and velocity. It is clearly enhanced by a factor two or more along collision lines, where the stationary updraft fronts confine the upward transport to a small area (Fuglestvedt & Haerter, n.d.). By contrast, the updrafts ahead of an expanding single CP lead to a moderate flux that is distributed over a larger area and is compensated by the downward circulation in the interior of the CP.

In combination, updraft strength and mass flux show that differences between two- and three-CP collisions are smaller than between a single CP gust front and a two-CP collision. This suggests that parameterisation schemes that aim at representing the effect of CPs on convection triggering, should distinguish between single CP gust fronts vs. locations of multi-CP collisions (Fig. 9b). The distinction between two- and three-CP collisions may however become important in strongly inhibited situations, where updrafts have to penetrate a layer of (conditionally) stable stratification near the top of the boundary layer. In such cases, the deeper updrafts in three-CP collisions may provide the required additional mechanical forcing (Grandpeix and Lafore (2010), Fig. 9a). The vicinity of pre-existing lines of enhanced horizontal convergence, e.g. from shallow con-

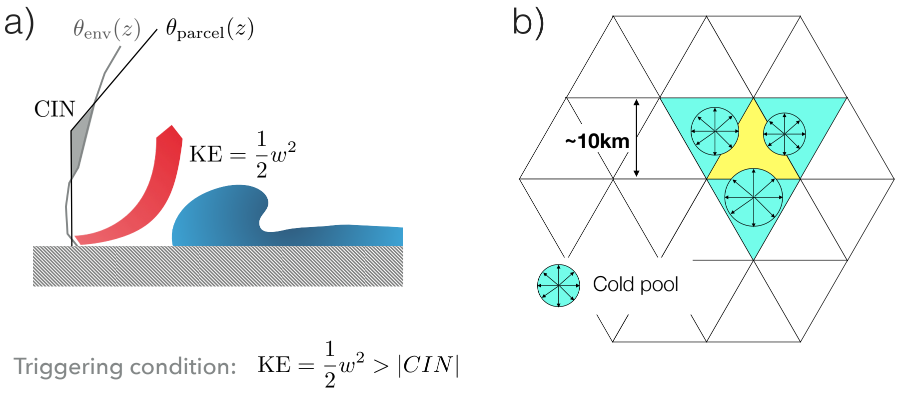

Figure 9. Cold pool parameterisation. a) The kinetic energy (KE) generated by cold pools allows updrafts to overcome a given convective inhibition (CIN) layer capping the boundary layer (adapted from: Grandpeix and Lafore (2010)). **b)** Role of cold pool collisions and nearest-neighbour interaction in convection parameterisation schemes for cloud-resolving models.

vection cells or sea breezes, is expected to have a similar effect and may further enhance this difference (Purdom, 1976). A particular future challenge might be posed by the emergence of mesoscale convective systems (Houze Jr, 2004), which appear to hinge of the formation of "combined cold pools" (Haerter et al., 2020), formed by rapid successions of multi-cold pool interactions — finally leading to the formation of a joint, deeper cold pool. Through their depth and large potential energy, these cold pools then act more autonomously, exciting subsequent updrafts near their periphery.

Altogether, the present study highlights the relevance of cold pool interactions. Our findings suggest, that the raincell - cold pool - raincell dynamics in populations of hundreds of raincells should be untangled and understood in terms of individual or multi-cold pool processes.

Appendix A LES Initialisation

A1 Initial Temperature Anomaly

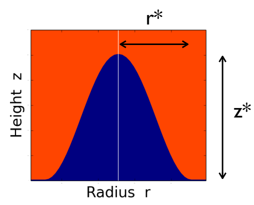

Figure A1. Initial configuration of cold pools in terms of a cold air 'mountain' of height z^* and base radius r^*

The cold pools are initialized as temperature anomaly of radius r^* and height z^*, centered at x_c, y_c.

$$\begin{aligned}
z_{max,0}(x,y) \quad &= z^* \cdot \cos^2\left[\frac{\pi}{2}\frac{\sqrt{(x-x_c)^2+(y-y_c)^2}}{r^*}\right] \\
&= z^* \cdot \cos^2\left[\frac{\pi}{2}\frac{r}{r^*}\right] = z_{max,0}(r), \\
z_{max,\delta}(x,y) \quad &= (z^*+\delta) \cdot \cos^2\left[\frac{\pi}{2}\frac{\sqrt{(x-x_c)^2+(y-y_c)^2}}{r^*+\delta}\right] \\
&= (z^*+\delta) \cdot \cos^2\left[\frac{\pi}{2}\frac{r}{r^*+\delta}\right] = z_{max,\delta}(r),
\end{aligned} \tag{A1}$$

The cos^2-envelope is chosen based on its positivity and symmetry with regard to zero.

A2 Potential Energy

The potential energy of a volume of cold air, as initialising the CPs, is computed as

$$\begin{aligned}
PE \quad &= g\int dV\,\frac{\theta'(\vec{x})}{\theta_0}\rho_d(z)\,z = g\frac{\theta'}{\theta_0}\int dV\,\rho_d(z)\cdot z \approx g\frac{\theta'}{\theta_0}\rho_0\int dV\,z \\
&= g\frac{\theta'}{\theta_0}\rho_0\,2\pi\int_0^{r_*} dr\,r\int_0^{z_{max}(r)} dz\,z \\
&= 2\pi\,g\frac{\theta'}{\theta_0}\rho_0\int_0^{r_*} dr\,r\,\frac{z_{max}(r)^2}{2} \\
&= \pi\,g\frac{\theta'}{\theta_0}\rho_0\int_0^{r_*} dr\,r\,z_*^2\cos^2\left[\frac{\pi}{2}\frac{r}{r_*}\right] \\
&= \pi\,g\frac{\theta'}{\theta_0}\rho_0(r_*z_*)^2\left(\frac{1}{4}-\frac{1}{\pi^2}\right) \propto \theta'(r_*z_*)^2.
\end{aligned} \tag{A2}$$

Following this formula, the **reference simulation** ($r^* = z^* = 1\,\mathrm{km}$, $\theta' = 3\,\mathrm{K}$) has an initial potential energy of $\mathrm{PE}_0 = 4.4\cdot 10^7\mathrm{kJ}$ (computed numerically from output fields of entropy; variances due to resolution from $\Delta x = 25$–$100\,\mathrm{m}$ only make a difference of less than 0.2%).

Appendix B Rain Intensities

The relation between rain intensity and initial PE of the CPs is approximated by computing how much energy needs to be extracted in order to cool the initial CP volume (i.e., the 3-dimensional volumes enclosed by the envelopes sketched in Fig. 5a) by a temperature drop θ'. Using an evaporation rate typical for tropical convection of $\eta = 20\%$ (Worden et al., 2007) and assuming an area and duration of the rain event, this energy can then be converted into a rain intensity. For simplicity, the area and duration of the rain events are assumed to be the same for all CPs, allowing only the intensity to vary.

A rain cell area equal to the initial area of the reference CP ($A = \pi(r_0^*)^2 \approx 3\mathrm{km}^2$) and a duration $\tau = 30\,\mathrm{min}$ is chosen. (*note:* since the initial anomaly is $\cos^2$-shaped, one could also use a mean width of this 'mountain' for r^*, reducing the area A and thus increasing the intensity I)

To cool a volume

$$V_{CP} = \int_0^{r^*} \mathrm{dr} \int_0^{z(r)} \mathrm{dz} = 2\pi(r^*)^2 z^* \left(\frac{1}{4} - \frac{1}{\pi^2}\right) \approx \pi/2(r^*)^2 z^*$$

by $T' = T'(\theta' = 3\mathrm{K})$, an amount Q of energy needs to be extracted

$$Q = c_{p,d} \int_{V_{CP}} \mathrm{d}V\, T'(\theta', p(z)) \cdot \rho_d(z).$$

This energy Q can be related to the latent heat absorbed when an amount of $m_w = Q/L_v$ water evaporates, where $L_v \approx 2500\,\mathrm{kJ/kg}$ is the specific latent heat of water at an ambient temperature of $0°C$ (Srivastava, 1985). We now assume that this water results from rain evaporated at a rate η in the sub-cloud layer below a rain cell of area A, which rains during a time τ at an intensity I

$$I = m_w/(\eta\, \rho_w\, \tau\, A),$$

where $\rho_w = 1000\mathrm{kgm}^{-3}$ is the liquid water density.

Appendix C Cold Pool Collisions

	neutral		stable	
separation d	t_{2CP}	t_{3CP}	t_{2CP}	t_{3CP}
10 km	1100 s	1500 s	1100 s	1500 s
12 km	1500 s	2200 s	1600 s	2300 s
15 km	2400 s	3300 s	2500 s	3600 s

Table C1. Collision times for the two sets of *3CP* simulations with neutral and stable background atmospheric profile ($\theta' = -5\,\mathrm{K}$, $z^* = 1\,\mathrm{km}$, $r^* = 1.1\,\mathrm{km}$).

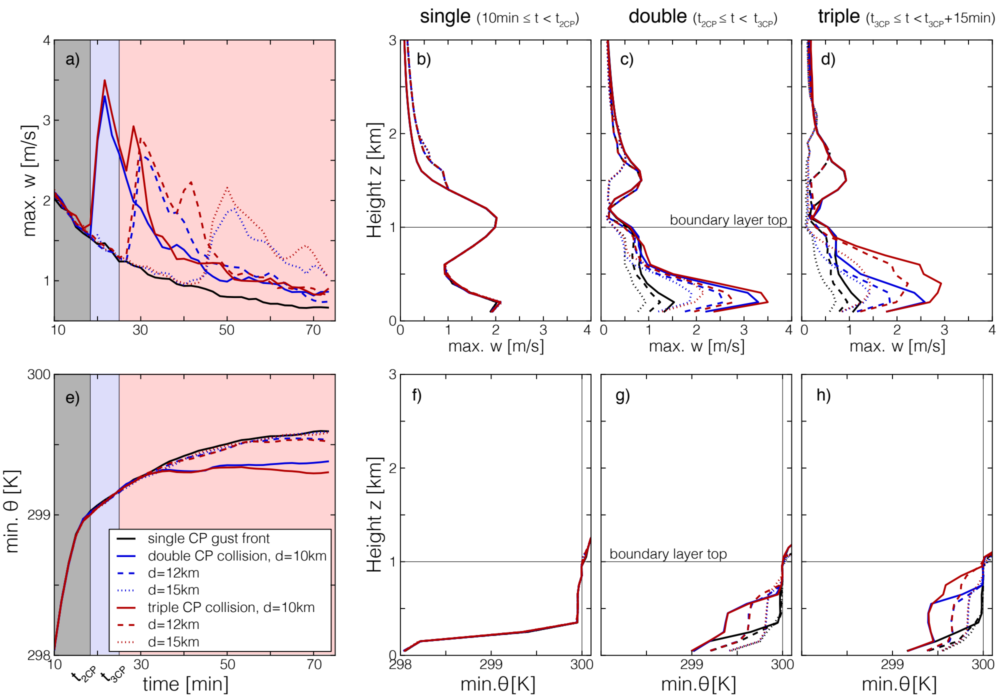

Figure C1. Same as in Fig. 7 but with stably stratified background.

Acknowledgments

The authors gratefully acknowledge funding by a grant from the VILLUM Foundation (grant number: 13168) and the European Research Council (ERC) under the European Union's Horizon 2020 research and innovation program (grant number: 771859). The authors acknowledge the Danish Climate Computing Center (DC3) and Roman Nuterman for technical support. Files to reconstruct the LES output code written for this article will be made available upon publication in a github repository. The PyCLES code used for the single cold pool simulation is accessible at this site (https://github.com/pressel/pycles). The initial configuration and namelist files will be made available upon publication. The cold pool tracking code used for measuring the cold pool radius is described in Henneberg et al. (2019) and available online (http://doi.org/10.5281/zenodo.3665813).

References

Addis, R. P., Garstang, M., & Emmitt, G. D. (1984). Downdrafts from tropical oceanic cumuli. *Boundary-Layer Meteorology*, *28*, 23–49. doi: 10.1007/BF00119455

Benjamin, T. B. (1968). Gravity currents and related phenomena. *Journal of Fluid Mechanics*(2), 109–248. doi: 10.1017/S0022112068000133

Cafaro, C., & Rooney, G. G. (2018). Characteristics of colliding density currents: A numerical and theoretical study. *Quarterly Journal of the Royal Meteorological Society*, *144*(715), 1761-1771. doi: 10.1002/qj.3337

Drager, A. J., & van den Heever, S. C. (2017, May). Characterizing convective cold pools. *Journal of Advances in Modeling Earth Systems*, *9*, 1091–1115. doi: 10.1002/2016MS000788.

Droegemeier, K., & Wilhelmson, R. (1985). Three-dimensional numerical modeling of convection produced by interacting thunderstorm outflows. part i: Control simulation and low-level moisture variations. *Journal of the Atmospheric Sciences*, *42*(22), 2381–2403. doi: 10.1175/1520-0469(1985)042⟨2381:TDNMOC⟩2.0.CO;2

Droegemeier, K., & Wilhelmson, R. (1987). Numerical simulation of thunderstorm outflow dynamics. part i: Outflow sensitivity experiments and turbulence dynamics. *Journal of the Atmospheric Sciences*, *44*(8), 1180–1210. doi: 10.1175/1520-0469(1987)044⟨1180:NSOTOD⟩2.0CO;2

Feng, Z., Hagos, S., Rowe, A. K., Burleyson, C. D., Martini, M. N., & de Szoeke, S. P. (2015). Mechanisms of convective cloud organization by cold pools over tropical warm ocean during the amie/dynamo field campaign. *Journal of Advances in Modeling Earth Systems*, *7*(2), 357–381. doi: 10.1002/2014MS000384

Fournier, M., & Haerter, J. O. (2019, September). Tracking the gust fronts of convective cold pools. *Journal of Geophysical Research: Atmospheres*, *124*(21), 11103-11117. doi: 10.1029/2019JD030980

Fuglestvedt, H. F., & Haerter, J. O. (n.d.). Cold pools as conveyor belts of moisture. *Geophysical Research Letters*, *n/a*(n/a), e2020GL087319. (e2020GL087319 2020GL087319) doi: 10.1029/2020GL087319

Grandpeix, J.-Y., & Lafore, J.-P. (2010, April). A density current parameterization coupled with emanuel's convection scheme. part i: The models. *Journal of the Atmospheric Sciences*, *67*, 881-897. doi: 10.1175/2009JAS3044.1

Grant, L. D., & van den Heever, S. C. (2016). Cold pool dissipation. *Journal of Geophysical Research: Atmospheres*, 1138–1155. doi: 10.1002/2015JD023813

Grant, L. D., & van den Heever, S. C. (2018). Cold pool-land surface interactions in a dry continental environment. *Journal of Advances in Modeling Earth Systems*, 1513–1526. doi: 10.1029/2018MS001323

Haerter, J. O., Berg, P., & Moseley, C. (2017, March). Precipitation onset as the temporal reference in convective self-organization. *Geophysical Research Letters*, *44*, 6450–6459. doi: 10.1002/2017GL073342

Haerter, J. O., Böing, S. J., Henneberg, O., & Nissen, S. B. (2019, May). Circling in on convective organization. *Geophysical Research Letters*, *46*, 7024–7034. doi: 10.1029/2019GL082092

Haerter, J. O., Meyer, B., & Nissen, S. B. (2020). Diurnal self-aggregation. *npj Climate and Atmospheric Science*, *3*, 30. doi: 10.1038/s41612-020-00132-z

Härtel, C., Carlsson, F., & Thunblom, M. (2000). Analysis and direct numerical simulation of the flow at a gravity-current head. part 2. the lobe-and-cleft instability. *Journal of Fluid Mechanics*, *418*, 213–229. doi: 10.1017/S0022112000001270

Henneberg, O., Meyer, B., & Haerter, J. O. (2019). Particle-based tracking of cold pool gust fronts. *Journal of Advances in Modeling Earth Systems*. doi: 10.1029/2019MS001910

Hirt, M., Craig, G. C., Schäfer, S. A. K., Savre, J., & Heinze, R. (2020). Cold pool driven convective initiation: using causal graph analysis to determine what convection permitting models are missing. *Quarterly Journal of the Royal Meteorological Society*. doi: 10.1002/qj.3788

Houze Jr, R. A. (2004). Mesoscale convective systems. *Reviews of Geophysics*, *42*(4). doi: 10.1029/2004RG000150

Kneller, B. C., Bennett, S. C., & McCaffrey, W. D. (1999, March). Velocity structure, turbulence and fluid stresses in experimental gravity currents. *Journal of Geophysical Research*, *104*(C3). doi: 10.1029/1998JC900077

Kurowski, M. J., Suselj, K., Grabowski, W. W., & Teixeira, J. (2018, December). Shallow-to-deep transition of continental moist convection: Cold pools, surface fluxes, and mesoscale organization. *Journal of the Atmospheric Sciences*, *75*(12), 4071–4090. doi: 10.1175/JAS-D-18-0031.1

Langhans, W., & Romps, D. M. (2015). The origin of water vapor rings in tropical oceanic cold pools. *Geophysical Research Letters*, *42*, 7825–7834. doi: 10.1002/2015GL065623

Leutwyler, D., Fuhrer, O., Lapillonne, X., Lüthi, D., & Schär, C. (2016). Towards European-scale convection-resolving climate simulations with GPUs: a study with COSMO 4.19. *Geoscientific Model Development*, *9*(9), 3393-3412. doi: 10.5194/gmd-9-3393-2016

Markowski, P., & Richardson, Y. (2010). *Mesoscale meteorology in midlatitudes.* John Wiley and Sons. doi: 10.1002/9780470682104

Nissen, S. B., & Haerter, J. O. (2020, Jan). Self-aggregation conceptualized by cold pool organization. *arXiv:1311.12849v2*.

Pressel, K. G., Kaul, C. M., Schneider, T., Tan, Z., & Mishra, S. (2015). Large-eddy simulation in an anelastic framework with closed water and entropy balances. *Journal of Advances in Modeling Earth Systems*, *7*(3), 1425–1456. doi: 10.1002/2015MS000496

Purdom, J. F. W. (1976, December). Some uses of high-resolution goes lmagery in the mesoscale forecasting of convection and its behavior. *Monthly Weather Review*, *104*, 1474–1483. doi: 10.1175/1520-0493(1976)104⟨1474:SUOHRG⟩2.0.CO;2

Romps, D. M., & Jeevanjee, N. (2016, April). On the sizes and lifetimes of cold pools. *Quarterly Journal of the Royal Meteorological Society*, *142*, 1517 — 1527. doi: 10.1002/qj.2754

Rooney, G. G. (2015). Descent and spread of negatively buoyant thermals. *J. Fluid Mech.*, *780*, 457–479. doi: 10.1017/jfm.2015.484

Rooney, G. G. (2018, October). Similarity-based approximations for the evolution of a gravity current. *Quarterly Journal of the Royal Meteorological Society*, *144*(716), 2302-2310. doi: 10.1002/qj.3371

Rotunno, R., Klemp, J. B., & Weisman, M. L. (1988, Feb). A theory for strong, long-lived squall lines. *Journal of the Atmospheric Sciences*, *45*(3), 463-485. doi: 10.1175/1520-0469(1988)045⟨0463:ATFSLL⟩2.0.CO;2

Schlemmer, L., & Hohenegger, C. (2014). The formation of wider and deeper clouds as a result of cold-pool dynamics. *Journal of the Atmospheric Sciences*, *71*, 2842–2858. doi: 10.1175/JAS-D-13-0170.1

Seifert, A., & Heus, T. (2013). Large-eddy simulation o organized precipitating trade wind cumulus clouds. *Atmospheric Chemistry and Physics*, *13*, 5631–5645. doi: 10.5194/acp-13-5631-2013

Simpson, J. (1980, April). Downdrafts as linkages in dynamic cumulus seeding effects. *Journal of Applied Meteorology*, *19*(4), 477–487. doi: 10.1175/1520-0450(1980)019⟨0477:DALIDC⟩2.0.CO;2

Simpson, J. E. (1972). Effects of the lower boundary on the head of a gravity current. *Journal of Fluid Mechanics*, *53*, 759-768. doi: 10.1017/S0022112072000461

Smagorinsky, J. (1963, January). General circulation experiments with the primitve equations. *Monthly Weather Review*, *91*(3), 99-164. doi: 10.1175/1520-0493(1963)091⟨0099:GCEWTP⟩2.3.CO;2

Srivastava, R. C. (1985). A simple model of evaporatively driven downdraft: Application to microburst downdraft. *Journal of the Atmospheric Sciences*, *42*(10), 1004–1023. doi: 10.1175/1520-0469(1985)042⟨1004:ASMOED⟩2.0.CO;2.

Tompkins, A. M. (2001a, July). Organization of tropical convection in low vertical wind shears: The role of cold pools. *Journal of the Atmospheric Sciences*, *58*, 1650–1672. doi: 10.1175/1520-0469(2001)058⟨1650OOTCIL⟩2.0CO;2

Tompkins, A. M. (2001b, March). Organization of tropical convection in low vertical wind shears: The role of water vapor. *Journal of the Atmospheric Sciences*, *58*, 529–545. doi: 10.1175/1520-0469(2001)058⟨0529:OOTCIL⟩2.0.CO;2

Torri, G., & Kuang, Z. (2019, January). On cold pool collisions in tropical boundary layers giuseppe. *Geophysical Research Letters*, *46*, 399–407. doi: 10.1029/2018GL080501

Torri, G., Kuang, Z., & Tian, Y. (2015, February). Mechanisms for convection triggering by cold pools. *Geophysical Research Letters*, *42*(6), 1943-1950. doi: 10.1002/2015GL063227

von Karman, T. (1940). The engineer grapples with nonlinear problems. *Bulletin American Meteorological Society*, *46*, 615–683. doi: 10.1090/S0002-9904-1940-07266-0

Wakimoto, R. (2001, 01). Convectively driven high wind events. In (p. 255-298). doi: 10.1007/978-1-935704-06-5_7

Worden, J., Noone, D., Bowman, K., Beer, R., Eldering, A., Fisher, B., … data contributors (2007). Importance of rain evaporation and continental convection in the tropical water cycle. *Nature*, *445*(7127), 528–532. doi: 10.1038/nature05508

Zhang, Y., & Klein, S. A. (2010, September). Mechanisms affecting the transition from shallow to deep convection over land: Inferences from observations of the diurnal cycle collected at the arm southern great plains site. *Journal of the Atmospheric Sciences*, *67*, 2943–2959. doi: 10.1175/2010JAS3366.1

Zuidema, P., Torri, G., Muller, C., & Chandra, A. (2017, November). A survey of precipitation-induced atmospheric cold pools over oceans and their interactions with the larger-scale environment. *Surveys in Geophysics*, *38*(6), 1283–1305. doi: 10.1007/s10712-017-9447-x